Monolayer molybdenum disulfide switches for 6G communication systems

Myungsoo Kim, Guillaume Ducournau, Simon Skrzypczak, Sung Jin Yang, Pascal Szriftgiser, Nicolas Wainstein, Keren Stern, Henri Happy, Eilam Yalon, Emiliano Pallecchi, et al.

Monolayer molybdenum disulfide switches for 6G communication systems

Myungsoo Kim[1], Guillaume Ducournau[2], Simon Skrzypczak[2], Sung Jin Yang[3], Pascal Szriftgiser[4], Nicolas Wainstein [5], Keren Stern[5], Henri Happy[2], Eilam Yalon[5], Emiliano Pallecchi[2] ✉ and Deji Akinwande [3] ✉

Atomically thin two-dimensional materials—including transitional metal dichalcogenides and hexagonal boron nitride—can exhibit non-volatile resistive switching. This switching behaviour could be used to create analogue switches for use in high-frequency communication, but has so far been limited to frequencies relevant to the fifth generation of wireless communi-cation technology. Here we show that non-volatile switches made from monolayer molybdenum disulfide in a metal–insulator–metal structure can operate at frequencies corresponding to the sixth-generation communication band (around 100–500 GHz). The switches exhibit low insertion loss in the ON state and high isolation in the OFF state up to 480 GHz with sub-nanosecond pulse switching. We obtain the eye diagrams and constellation diagrams at various data transmission rates and modulations to evaluate the device performance, including real-time data communication up to 100 Gbit s^{-1} at a carrier frequency of 320 GHz, with a low bit error rate and high signal-to-noise ratio.

Analogue switches are ubiquitous components in data communication systems, and are used to pass or isolate analogue and digital signals between different frequency bands and reconfigure wireless communication systems[1–14]. One of the most critical performance criteria is energy consumption. Conventional analogue and radio-frequency (RF) switches based on solid-state diode or transistor devices[4–6] are volatile and consume energy during switching events and also during standby or when idle in the ON and OFF states. The former is the dynamic energy that is needed to toggle the states, whereas the latter is the static energy consumption and represents wasted energy. To substantially reduce the overall energy consumption, non-volatile memory devices such as memristors, resistive random-access memory (RRAM), phase-change memory (PCM) and two-dimensional (2D) atomristors and memristors have been explored due to their zero static energy consumption[9–21].

We previously reported molybdenum disulfide (MoS_2) switches operating at microwave frequencies (up to 50 GHz)[21] and hexagonal boron nitride (hBN) switches operating across the entire fifth-generation (5G) spectrum (100 GHz), with data rates of 8.5 Gbit s^{-1} using on–off keying modulation. These 2D analogue switches outperform switches based on other emerging materials—including PCM, RRAM and microelectromechanical devices—in terms of energy efficiency, cutoff-frequency figure of merit, switching speed and switching voltages, despite their relatively nascent state[21–23]. However, next-generation wireless communication technologies based on the evolving sixth-generation (6G) standard[24,25] will require higher operating frequencies (carrier frequencies of around 300 GHz) and more sophisticated modulation schemes, with data rates approaching 100 Gbit s^{-1}. This is needed to support existing mobile networks and enable new applications such as virtual/augmented reality and artificial intelligence with enhanced security and privacy[26–28].

In this article, we report non-volatile analogue switches based on metal–insulator–metal (MIM) memristor structures[29–31] with monolayer MoS_2 as the resistive switching insulator. The switches exhibit enhanced performance compared with previous 2D-material-based switches, including an operation bandwidth of 480 GHz, which we demonstrate using a sophisticated high-frequency measurement setup that includes various frequency extenders, impedance substrates, vector network analysers (VNAs) and probe sets. We attribute this enhancement to the area-scaling benefit of the vertical parallel-plate capacitance structure and coplanar waveguide (CPW) design optimization. In particular, by downscaling the device dimensions to 0.04 μm^2 (6.25 times smaller than the previous report[21]), the OFF-state capacitance was reduced from 6.5 to 0.9 fF. The high-frequency properties are validated using various modulation methods and with measurements of the eye diagram, constellation diagram, bit error rate (BER) and signal-to-noise ratio (SNR). A sub-nanosecond switching time of 500 ps is achieved and the corresponding switching energy of 50 pJ is more than one order of magnitude lower than mature PCM RF switches[1,2]. We also demonstrate data transmission rates as high as 100 Gbit s^{-1}, fulfilling 6G communication requirements. Furthermore, we achieve real-time high-definition (HD) television (TV) streaming with no compression (1.5 Gbit s^{-1}) at a carrier frequency of 300 GHz. RF intermodulation measurements (IMD) show that the MoS_2 memristor RF switches exhibit a third-order intercept point (IP3)—an important metric for distortion-less communication systems—of around 31 dBm.

Structure, material properties and resistive switching. Figure 1 shows the device structure, material properties and d.c. and pulse resistive switching of a monolayer MoS_2 switch fabricated on a 300-μm-thick polycrystalline diamond substrate. The diamond

[1]Department of Electrical and Computer Engineering, Ulsan National Institute of Science and Technology (UNIST), Ulsan, South Korea. [2]IEMN, University of Lille, Villeneuve d'Ascq, France. [3]Microelectronics Research Center, The University of Texas at Austin, Austin, TX, USA. [4]Université de Lille, CNRS, UMR 8523—PhLAM—Physique des Lasers Atomes et Molécules, Lille, France. [5]Technion, Israel Institute of Technology, Haifa, Israel. ✉e-mail: emiliano.pallecchi@univ-lille.fr; deji@ece.utexas.edu

https://doi.org/10.1038/s41928-022-00766-2

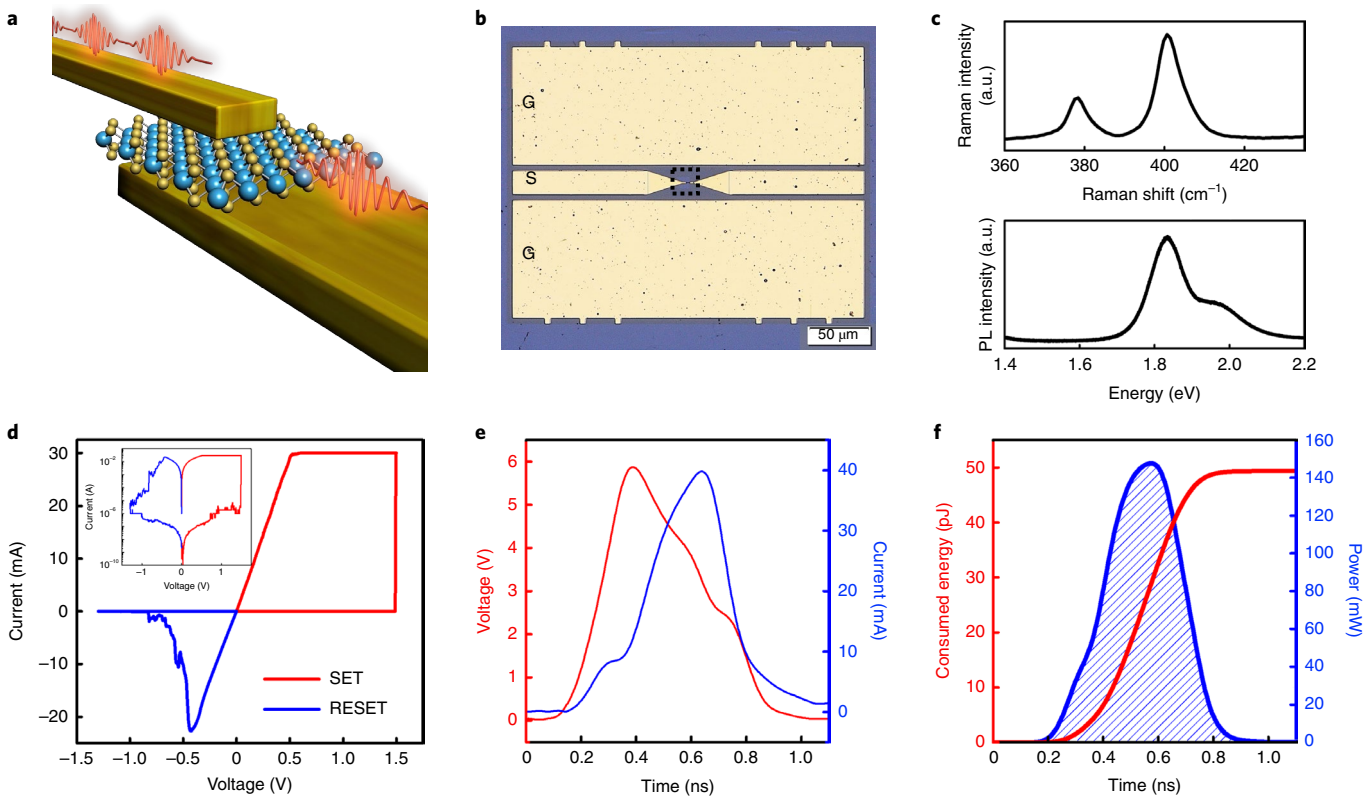

Fig. 1 | Material, device structure, and d.c. and pulse switching. a, Simplified perspective-view illustration of the MoS_2 RF switch with a vertical MIM structure. **b**, Optical microscopy image of a fabricated monolayer MoS_2 RF switch with GSG Au electrodes. The dashed box shows the vertical MIM structure. **c**, Raman spectroscopy and PL data of CVD-grown monolayer MoS_2. **d**, Typical *I*–*V* curve of the resistive switching behaviour of monolayer MoS_2 device with an overlap area of $0.5 \times 0.5\,\mu m^2$. **e**, Voltage and current through the switch with a 500 ps, 5 V SET pulse. The current is measured as the pulse is applied using a scope in series (Methods describes the voltage calculations). **f**, Consumed energy and power during the 500 ps SET pulse. The consumed energy is calculated by integrating the power over time. The measured SET energy is 49 pJ.

substrate was chosen to provide efficient heat sinking to the device switching area and metal feedlines during d.c. and RF operations. We created an array of devices, and 36 out of the 38 devices functioned as memristors based on d.c. testing, resulting in about 95% yield. Figure 1a,b shows an illustration and top-view optical image of a ground–signal–ground (GSG) device configuration of the MoS_2 analogue switch with Au electrodes. Supplementary Fig. 1 shows the zoomed-in top-view optical image of the dashed box shown in Fig. 1b, with the colour difference indicating the area covered with MoS_2. The overlap between the BE and TE defines the switch area, which is $0.2 \times 0.2\,\mu m^2$. The switch stack consists of ~150 nm gold (Au) TE and BE, both with 2 nm chromium (Cr) adhesion layers. First, BEs with the GSG configuration were formed by lift-off after electron-beam lithography (EBL) and electron-beam metal evaporation. Then, chemical-vapour-deposited (CVD) monolayer MoS_2 is transferred onto the BE using poly(methyl methacrylate)-assisted wet transfer[29,32]. Finally, the TE was prepared using the same fabrication process as the BE. Raman spectroscopy and photoluminescence (PL) of the CVD-grown MoS_2 film confirm the crystalline quality and monolayer thickness (Fig. 1c). Figure 1d shows the linear and log-scale current–voltage (*I*–*V*) curves of the fabricated MoS_2 switch, exhibiting bipolar non-volatile resistive switching phenomena. The device is initially in the high-resistance state[15]. The positive voltage sweeps from 0 to 1.5 V and then returns to 0 V, followed by a negative bias of 0 to −1.5 V. Applying d.c. voltage as the stimulus shows a sudden increase (SET process) in the current at around 1.5 V (Fig. 1d), which corresponds to a low-resistance state. The device retains its resistance state (non-volatility) until a negative voltage is applied to RESET the device back to its initial high-resistance state. The non-volatile resistive switching of 2D-material-based monolayer memristors is attributed to an atomic virtual conductive-point mechanism, which have been verified by first-principles calculations and scanning tunnelling microscopy studies in recent reports[33,34]. Field-driven metal-ion adsorption into chalcogen vacancies results in a locally conductive site, thereby enabling the non-volatile resistive switching phenomenon. Supplementary Fig. 2 depicts the *I*–*V* curves of the SET processes, as well as its normal probability plot for the ON-state resistance for nine different MoS_2 switches with an identical compliance current. The high-speed switching experimental setup is shown in Supplementary Fig. 3 with a pulse generator (PG) connected in series with the MoS_2 memristor and high-speed oscilloscope. Figure 1e represents the graph of voltage and current versus time of 500 ps SET pulse switching on monolayer MoS_2 memristor from the OFF state to the ON state. The consumed power and switching energy during the SET switching event are shown in Fig. 1f. Similarly, Supplementary Fig. 4 shows the 500 ps RESET pulse switching of the MoS_2 device.

High-frequency performance studies. Here S-parameter measurements were conducted using a VNA and frequency converters in both ON and OFF states of the analogue switch based on MoS_2 memristors. To measure the precise S-parameters, line–reflect–reflect–match on-wafer calibration was conducted to remove the extrinsic effects from the cables and probe station. For each individual frequency band, the VNA's error coefficients of the 12-term error model are calculated using WinCal software

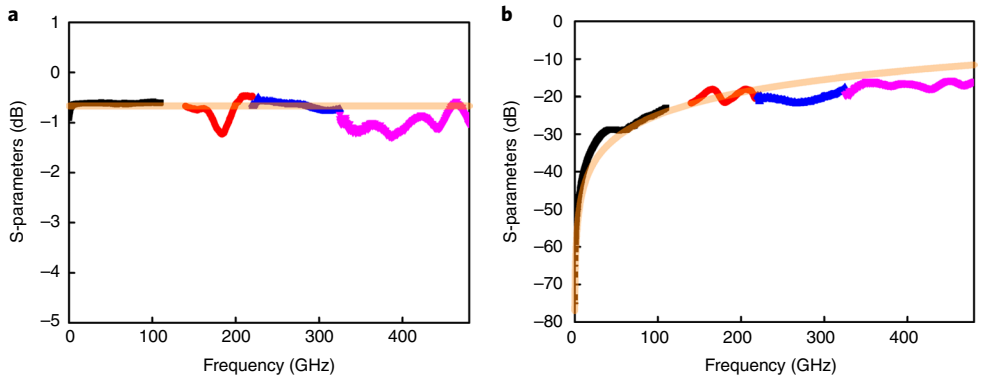

Fig. 2 | High-frequency THz performance of MoS_2 non-volatile switch. a,**b**, De-embedded experimental S-parameter S_{21} data in the ON (insertion loss) (**a**) and OFF (isolation) (**b**) states of a 6G switch. The SET and RESET data are measured on devices with an overlap area of $0.2 \times 0.2\,\mu m^2$. The black, red, blue and magenta colour lines show the S_{21} data of the 0.25–110.00, 140.00–220.00, 220.00–325.00 and 325.00–480.00 GHz bands, respectively. The orange lines show the S-parameters of the extracted equivalent lumped element circuit model. The extracted R_{ON} and C_{OFF} values are 8 Ω and 0.9 fF and the calculated cutoff frequency, F_{CO}, is 22 THz.

from the S-parameter measurements of one line, two reflect and one match structure on commercial calibration substrates from FormFactor. To avoid artefacts in our measurements, the stability of the calibration was monitored after each device and new calibration is performed when necessary (drift in S-parameters measured on a calibration structure larger than 0.1 dB compared with the same structure measured right after calibration or appearance of noise-like ripples at high frequency). Also, probe pads and interconnect resistances were removed by de-embedding processes to obtain the intrinsic S-parameters of MoS_2 switches[35]. Using a sophisticated probe-station setup, the intrinsic experimental high-frequency characteristics of monolayer MoS_2 switch show a small insertion loss in the ON state (Fig. 2a) and isolation below 15 dB in the OFF state (Fig. 2b) at frequencies up to 480 GHz, which is in the terahertz (THz) range usually defined at around 0.1–10.0 THz. Based on the equivalent lumped element circuit model, two circuit parameters[12,36], namely, R_{ON} (ON-state resistance) and C_{OFF} (OFF-state capacitance), were extracted from the de-embedded experimental data[23] to obtain their quasi-static values (Supplementary Fig. 5 and Supplementary Note 1). The comparison between the measured results and the intrinsic lumped element model is presented for the ON state (Fig. 2a) and OFF state (Fig. 2b). Metal–oxide RRAMs are typically realized with amorphous transitional metal oxides with low-resistance-state values of >1 kΩ, making them unsuitable for RF switching due to excessive insertion losses. PCM RF switches[13,14], on the other hand, have shown outstanding results with high endurance and a decent cutoff frequency with low ON-state resistance. However, due to heat transfer, they have very long switching times, require an integrated heater for electrothermal actuation and have adverse area dependency that limits scalability to higher frequencies. Vanadium dioxide (VO_2) is a phase-change material with an insulator–metal transition (IMT)[17,37–39]. VO_2 is an intriguing material for RF switches due to the high resistance difference between the insulating and metallic phases, as well as low resistivity in the metallic phase. However, this sudden, reversible and volatile IMT occurs at the transition temperature (68 °C) and necessitates higher temperatures to maintain the conducting state, whereas the material operates as an insulator at ambient temperature. Furthermore, 2D-material-based memristors achieve small ON-state resistance of <10 Ω due to their thin transport layer. Also, a small OFF-state capacitance is realized by MIM area scaling, a benefit of the vertical parallel-plate capacitance structure. Notably, unlike conventional RF switches, where the insertion loss rolls off with frequency due to inductive effects, the 2D switch exhibits a relatively flat insertion loss with frequency owing to a parallel-plate capacitive effect in the nanoscale MIM structure[22,23]. Supplementary Fig. 6 shows the reliable retention of two different MoS_2 RF switches in the ON and OFF states over a nine-month period. The performance of 2D-material-based RF switches is compared with that of other RF switch technologies such as PCM, conductive-bridge RAM, resistive RAM, IMT and microelectromechanical systems. Although 2D RF switches are still in their early development phases, they outperform other technologies in several important metrics including higher operating frequency, higher data transmission, heater-free ambient integration and fast switching speed (Supplementary Table 1).

Data communication studies based on BER and SNR measurements. Using THz photonics devices, several modulations were tested to evaluate the response of the MoS_2 device towards the IEEE 802.15.3d standard[24]. Since 6G communication technologies can be integrated with many application scenarios, it must be versatile.

To evaluate the device potential on high-bandwidth applications, real-time data communication tests were conducted on MoS_2 switches with a carrier frequency (f_c) of 320 GHz. The measurement setup[23] is shown in Supplementary Fig. 7 and Supplementary Video 1. Figure 3a represents the real-time BER measurement as a function of the input power at different switch statuses with 10 Gbit s^{-1} data-rate amplitude-shift keying (ASK) modulation. For the THRU and ON state, the eye diagrams and the evolution of BER values are similar. The gap between the THRU and ON state reveals the power losses from the small insertion loss of the MoS_2 switch over the modulated signal. BER measurements with on–off keying modulation at data rates of 18 and 22 Gbit s^{-1} have similar evolutions (Supplementary Fig. 8).

In terms of data transmitting and receiving performances, a combination of high baud rate/spectral efficiencies and multilevel modulations are required. In this context, the functionality of the MoS_2 switch was validated using quadrature phase-shift keying (QPSK) for 10 and 25 GBaud (20 and 50 Gbit s^{-1}, respectively); amplitude–phase-shift keying (APSK) with 16 symbols (APSK16); and quadrature amplitude modulation (QAM) with 16, 32 and 64 symbols (QAM16, QAM32 and QAM64, respectively). The evolution of SNR values for different modulation methods and data rates is shown in Fig. 3b. For higher data rates, all the modulation methods show decreasing SNR trend, which is due to the limitation of the transmitting and receiving hardware available at the time of experiments. For QAM16, the data rate was successfully upgraded to 100 Gbit s^{-1}, which is the target of the new IEEE 802.15.3d release

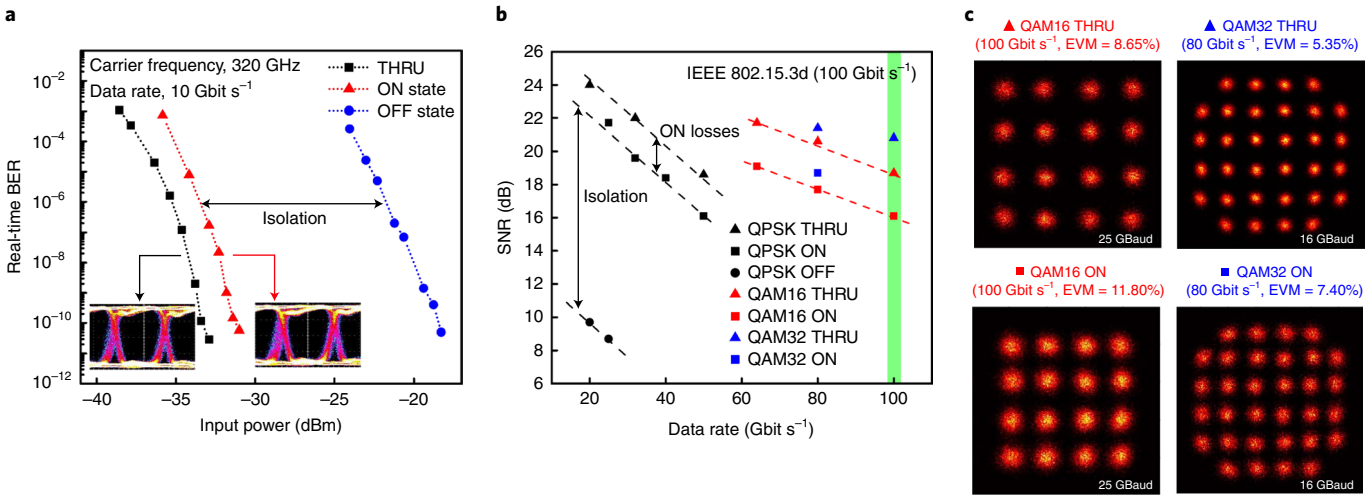

Fig. 3 | Data communication measurements. a, Real-time BER measurement with different switch statuses using ASK modulation. The inset shows the eye diagrams of the THRU and ON state measured at a carrier frequency of 320 GHz with a bit rate of 10 Gbit s^{-1}. **b**, SNR graph shows the good signal quality at various data rates with different modulation methods. The green band at 100 Gbit s^{-1} is the data rate of the 6G standard (IEEE 802.15.3d). **c**, QAM16 and QAM32 constellation diagrams for devices with the THRU and ON state.

for 6G networks using the 300 GHz band. It should be noted that high-level QAM64 modulation was also successfully handled by the MoS_2 switch, which is also a potential modulation technique in the IEEE 802.15.3d standard for future THz communication. These results show the broadband operation of the device: for the highest baud rates, for example, using 25 GBaud, the spectrum has a bandwidth close to ~40 GHz. Considering the carrier frequency at 320 GHz, the RF signal injected into the MoS_2 switch is, thus, spread over the 300–340 GHz range; even for such wideband signals, a successful operation of the switch was obtained. The bandwidth of the modulated spectrum was finally compliant with the 51.84 GHz bandwidth of channel 68 of the new standard[40]. However, the demonstration was conducted using a 320.00 GHz carrier rather than a 278.64 GHz (IEEE standard), due to device availability (that is, the Schottky receiver) at the time of the experimental measurements. It should be noted that as the response of the MoS_2 switch is less lossy at 280 GHz, the performance would be even better.

Figure 3c represents the constellation diagram of QAM16 and QAM32 modulation at the THRU and ON state. For the same modulation method and data rate, the error-vector magnitude (EVM) of THRU is less than the EVM of the ON state, showing less noise and distortion. Supplementary Fig. 9a shows the SNR-signal detection limitation for each modulation method due to hardware specifications, and as a result, only the OFF state could be measured for QPSK. Accordingly, Supplementary Fig. 9b shows the constellation diagram of QPSK modulation with the THRU, ON and OFF states. The EVM values for different modulation methods and data rates are shown in Supplementary Fig. 10.

Based on the S-parameter measurements with VNAs, it was discovered that the switches have a very small amount of dispersion, allowing them to be considered as pure controllable attenuating devices for a specific frequency range with two states, namely, ON and OFF. This was confirmed in both real-time BER (Fig. 3a) and in-phase/quadrature (I/Q) measurements (Fig. 3b), where the BER and SNR curves comparing the THRU/ON/OFF state (ASK and QPSK) were found to be parallel, with the power penalty (decibel shift between the curves) equal to the insertion losses. This implies that unlike active devices, 2D switches have no effect on signal integrity or additional noise aside from power reduction. Thus, the influence of the MoS_2 layer was found to be limited to pure signal-power reduction, reducing the SNR according to the signal loss, with the noise level remaining constant as fixed by the receiver in any case.

Eye diagrams with various modulation methods. Figure 4 shows the data communication performance on MoS_2 devices with different data rates and modulation methods using eye diagrams. From Fig. 4a, the green band at 100 Gbit s^{-1} shows the data-rate target of IEEE 802.15.3d, which is the IEEE standard for high data-rate wireless multimedia networks (amendment) towards emerging 6G applications (expected for 2030). Figure 4b shows the representative constellation diagrams and eye diagrams from Fig. 4a; the blue histograms under the eye diagrams show the signal-crossing probabilities between the eye-diagram levels. A zero value of this curve at the decision instant (normalized time = 1 in the eye patterns) means that the probability of error is zero. When the EVM is reduced and the eye starts to close, this probability increases. Here the EVM values are considered as figures of merit of the constellations, since BER is not measured in real time for I/Q modulation.

Once the high data-rate characterizations with I/Q arbitrary generation and analysis are conducted, the real-time high-data-rate applications were studied. The real-time performance of the BER is detected with a BER tester that directly compares the data flow at the input and output of the MoS_2 device. In the ON state, an HDTV data stream encoded into the 300-GHz-band carrier without any compression (1.5 Gbit s^{-1}) was successfully transmitted through the MoS_2 device. Then, it was decoded and displayed in real time on a TV without any latency (Supplementary Note 2 and Supplementary Video 1). When the device is electrically switched into the OFF state, data transmission is interrupted, and the real-time TV stream disappears. This demonstration confirms that the full operation of the switch handles the real-time data streams encoded in the THz bands for 6G applications.

Nonlinearity measurement. Intermodulation distortion measurement (IMD) is used to evaluate the nonlinearity of high-frequency devices. MoS_2 RF switches exhibit good linearity when the fundamental signal and third-order intermodulation product are compared with the IMD visual guideline with slopes of 1 and 3, respectively. When the power of the input RF signal is increased, nonlinearity can occur. According to previous research, as the compliance current increases, the ON-state resistance decreases[22,23].

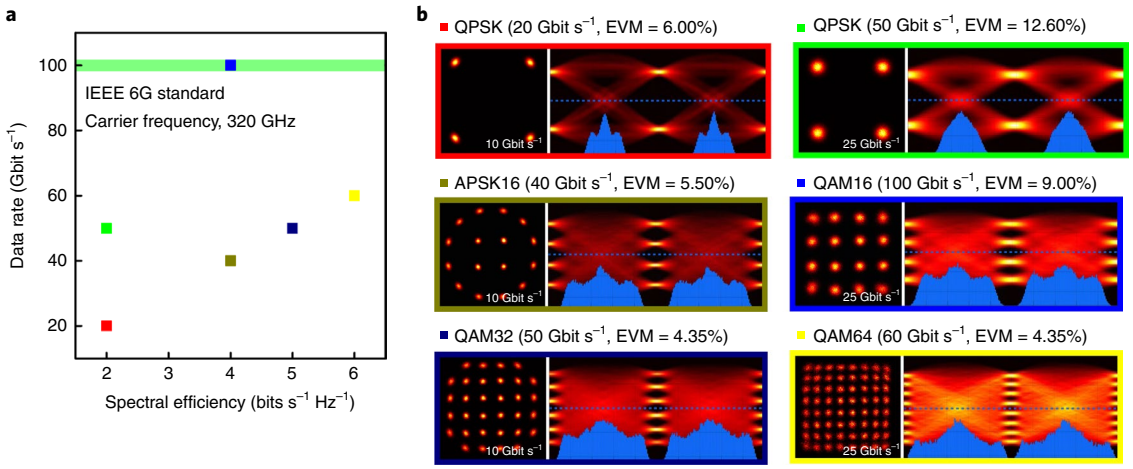

Fig. 4 | Eye diagrams with different data rates and modulation methods. a, Data communication measurement on MoS_2 switch at different data rates and modulation methods. The green band at 100 Gbit s^{-1} conforms to IEEE 802.15.3d—the IEEE 6G standard for high data-rate wireless multimedia networks. **b**, Representative constellation diagrams and eye diagrams from **a**. The blue spectrums under the eye diagrams show the eye-crossing section.

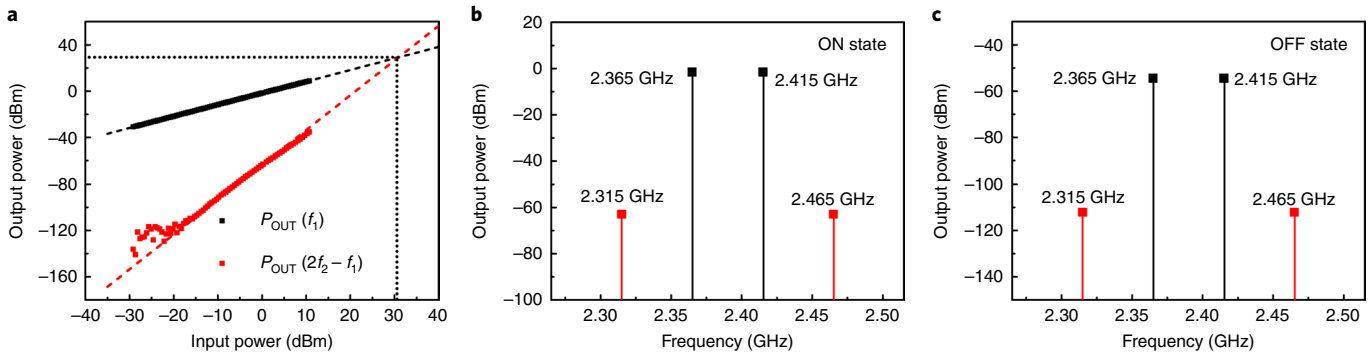

Fig. 5 | Nonlinearity characteristics of MoS_2 RF switches. a–**c**, IMD measurement at the ON and OFF states to evaluate the linearity of MoS_2 devices (f_1, 2.365 GHz; f_2, 2.415 GHz; $2f_2 - f_1$, 2.465 GHz). The IMD measurement indicates IIP3 of 31 dBm and OIP3 of 30 dBm in the ON state. The black and red dashed lines represent the visual guides for IMD measurement (**a**). The slopes of the guide lines in the ON-state IMD measurement are 1 and 3, indicating the power slope of the fundamental signal and third-order intermodulation product, respectively (**b**). The output-power spectrum of the IMD measurement in the ON state (P_{IN} = 0.26 dBm with −61.43 dBc) (**b**) and OFF state (P_{IN} = 0.08 dBm with −57.72 dBc) (**c**).

Since the high RF input power can induce self-heating (which impacts the electrical properties), the ON-state resistance variation can cause nonlinearity. The VNA is used to generate and inject the two input tones (f_1 = 2.365 GHz and f_2 = 2.415 GHz) into the device, with a power sweep from −30 to +10 dBm. Figure 5a shows the IMD graph of the input (f_1) and third-order intermodulation ($2f_2 - f_1$) signal with 31 dBm input IP3 (IIP3) and 30 dBm output IP3 (OIP3) in the ON state. Figure 5b represents the spectrum of the output signals in the ON state with input power $P_{IN}(f_1)$ = 0.26 dBm, output powers $P_{OUT}(f_1)$ = −1.53 dBm and $P_{OUT}(2f_2 - f_1)$ = −62.96 dBm. Similarly, Fig. 5c shows the OFF-state spectrum with P_{IN} = 0.08 dBm, $P_{OUT}(f_1)$ = −54.45 dBm and $P_{OUT}(2f_2 - f_1)$ = −112.17 dBm. Supplementary Fig. 11a,b shows the IMD measurements at the THRU and ON state and the OPEN and OFF state, respectively.

Conclusions

We have reported nanoscale non-volatile analogue switches based on monolayer MoS_2 for applications in 6G data communication. The high-frequency switches achieve low insertion loss and high isolation up to 480 GHz due to their nanoscale vertical and lateral dimensions, which results in low resistance in the ON state and low capacitance in the OFF state, respectively. The devices achieved a data rate of 100 Gbit s^{-1} (conforming to the IEEE 6G standard for high-frequency components), with low EVM, low BER and high SNR. The eye diagram and constellation diagram measurements using various complex modulation methods substantiate the high performance of the MoS_2 switches. In addition, the IMD measurements revealed linearity with an IP3 value of 31 dBm. These results show that MoS_2-based non-volatile analogue switches could be a valuable component in high-data-rate 6G data communication and related systems.

Methods

Device fabrication and characterization. The MoS_2 memristors were fabricated on a 0.3-mm-thick polycrystalline CVD diamond substrate (Element Six; thermal conductivity of >1,000 W m^{-1} K^{-1}). The 50-μm-pitch GSG device configuration was patterned by EBL. An electron-beam metal evaporator was used to deposit the ground pads and the BE consisting of 2-nm-thick Cr for the adhesion layer and 100-nm-thick Au. CVD-grown monolayer MoS_2 (2D Semiconductors) was transferred to the fabricated BE using a poly(methyl methacrylate)-assisted wet transfer method. Then, EBL and plasma-etching processes defined the active region of the MoS_2 film. Last, the TE was patterned and deposited by using the same fabrication process as the BE. The d.c. measurement was conducted on a FormFactor probe station with a Keysight 4156 semiconductor parameter analyser under ambient conditions. The Renishaw inVia system with a 532 nm wavelength source was used to obtain the monolayer MoS_2 Raman spectroscopy and PL data.

High-speed pulse-switching measurements. The high-speed switching experimental setup (Supplementary Fig. 2) consists of an Active Technologies

Pulse Rider PG-1072 PG connected in series with the memristor and a Keysight Infiniium DSOS804A high-speed oscilloscope. The device is probed using GGB model 40A GSG probes, which are connected to the CPW where the MoS_2 memristors were fabricated. The output impedance of the PG, scope and characteristic impedance of the CPW are $Z_0 = 50\,\Omega$. First, the voltage pulses are applied to a CPW THRU structure (that is, a structure without the MoS_2 memristor) to obtain the transient response from the PG to the scope, applied to the cables, RF probes and device leads. Then, $V_{PG,SET}$ and $V_{PG,RESET}$, the voltage applied by the pulse generator during SET and RESET operation, with varying amplitudes (–5 to 5 V) and widths (0.5 to 5.0 ns) are applied. The current through the switch ($I(t)$) is calculated as $I(t) = V_S(t)/Z_0$, where $V_S(t)$ is the voltage measured at the scope. Thus, the transient voltage at the device (V_{DUT}) can be expressed via Kirchhoff's voltage law as $V_{DUT} = V_{PG,APP} - I(t)(Z_0 + R_s) - V_S(t)$, where $V_{PG,APP}$ is the voltage applied by the PG to a 50 Ω load ($V_{PG,APP} = 2V_{PG,SET} \times R_{DUT}/(R_{DUT} + Z_0)$), R_{DUT} is the device resistance, and R_s is the series resistance of the leads and cables. Finally, the resistance of the device is read with a d.c. bias voltage of 0.1 V to assert that the state has changed.

RF measurements. High-frequency characteristic measurements were conducted using a Keysight E5270 source meter unit and various VNAs with FormFactor GSG probes at a pitch of 100 or 50 µm. Also, R&S ZVA110 and Agilent E8361A VNAs were used to cover the 0.25–110.00 GHz range. Furthermore, R&S ZVA24 with frequency converters covered the 140–220, 220–325 and 325–480 GHz bands. The device was placed on top of an absorber (FormFactor) to avoid any coupling to the sample holder. The power of the RF source was set to –16 dBm, which is in the small-signal range for S-parameter measurements to prevent nonlinear effects. To obtain precise results and remove the parasitic effects of impedances arising from the cables and probe station, line–reflect–reflect–match calibration—one of the on-wafer calibration methods—was carried out up to 480 GHz using a Cascade calibration kit and WinCal software (FormFactor)[41]. The S-parameters were measured in the ON and OFF states. Since the MoS_2 device has a non-volatile resistive switching characteristic, we applied forward and reverse d.c. biases to turn on and off the switching device, respectively. Then, the S-parameters were measured in the ON and OFF states, respectively. An open-short de-embedding process was used to remove the pad and interconnect resistances.

Data communication testing. Two different experimental setups have been used to qualify the capability of the MoS_2 switches in different scenarios. The first is amplitude modulation for ultralow-latency networks and the second used complex signal manipulation with the switch, targeting future 100 Gbit s^{-1} communication in 0.3 THz bands identified as an enabling technology for 6G core networks. As low-latency/real-time systems are one of the drivers of future 6G networks, the first scenario was to consider amplitude modulation tests with real-time BER performance evaluation, without any signal processing or dispersion compensation. In this first setup, two tunable lasers were used to generate a dual-tone signal in the optical domain, with 320 GHz frequency separation. These two tones were amplitude modulated inside a Mach–Zehnder modulator optimized for amplitude modulation. After the optical amplification stage, the dual-tone-modulated optical signal was injected inside the optical-to-THz converter (photomixer). The photomixer was a unitravelling-carrier photodiode with waveguide output. This photodiode realized the photomixing of the two optical tones to generate a 320 GHz modulated signal, corresponding to the frequency difference of the two optical tones. A waveguide probe (T-Wave) was used to inject the modulated 320 GHz signal using coplanar topology (GSG footprint with 50 µm separation between the centre of the contacts) to feed the MoS_2 switch. At the switch output, a second GSG probe was used to feed the 320 GHz receiver composed of amplification stages and Schottky-barrier diode for envelope (direct) detection. Envelop detection enables baseband (binary) data detection in real time, that is, without any signal processing or offline process. The output of the receiver was then directly fed to a BER tester to measure the real-time BER performance. In this case, we were able to evaluate the switch impact (ON losses) by comparison between simple THRU (same footprint) and the switch isolation factor corresponding to the power penalty between ON and OFF for a given BER value. The slopes of the BER curves were found to be the same, confirming the losses (power shift between the curves), but no further degradations (distortions) were introduced (same slope curve). This measurement enabled to conduct the full-functional switch operation with real-time data flow. After the test was conducted with random data, real-time HD video fluxes were used to confirm the transmission inside the switch. Such modulation schemes offer the advantage of avoiding complex signal processing at the receiver level, thereby leading to the better energy efficiency of the whole system—a key point for 6G applications.

Beyond amplitude modulation/low-latency operation, a second experimental setup was used to evaluate the switching behaviour with high-complexity modulated THz channels as targeted by the IEEE 802.15.3d standard for 300-GHz-band communication. In this case, the setup was composed of arbitrary waveform generation of two baseband data signals obtained from a Keysight M8195A enabling up to 25 GBaud generation. These two baseband signals were then fed to an optical I/Q Mach–Zehnder modulator to modulate a 193.1 THz optical signal using amplitude/phase modulation. By adjusting the baseband type of the Mach–Zehnder modulator, several modulation formats could be generated in the optical domain (QPSK, QAM16, QAM32 and QAM64). This modulated optical signal was then combined with a continuous-wave optical laser line at 193.42 THz. These optical signals, after amplification inside an erbium-doped amplifier, were fed to the same THz photomixer and then the same probing system. To ensure the detection of complex modulations, at the switch output, the second GSG probe was fed to a different receiver; in this case, it was a waveguide heterodyne receiver composed of a Schottky-barrier sub-harmonic mixer working at 320 GHz and pumped by a 150 GHz local oscillator. At the mixer output, a 20 GHz intermediate-frequency signal is amplified with a distributed amplifier (SHF810) to feed a wideband real-time oscilloscope. The detected signals are finally analysed using offline signal processing and equalized to remove the dispersion of the receiver, which is mostly dominated by the frequency evolution of the intermediate-frequency path inside the sub-harmonic mixer and coaxial connection from the receiver to the oscilloscope. The output parameters of the offline analysis are the SNR, constellation diagrams, eye diagrams and EVM.

IMD measurement. The third-order intermodulation of a two-tone test was measured with a probe station equipped with Picoprobe GSG probes and Keysight N5222A VNA. An HP8564E spectrum analyser was added for real-time visual monitoring of the signal levels. The VNA is used to generate the two input tones and measure the signal-power levels. The VNA power calibration was performed using a bolometer for the input port and a calibrated source for the output port; the losses of the probes were determined by S-parameters. During the measurements, two signals ($f_1 = 2.365$ GHz and $f_2 = 2.415$ GHz) are injected into the device
input port and their power is swept from –30 to +10 dBm. The output signals at frequencies of 2.365 GHz, 2.415 GHz and 2.465 GHz ($2f_2 - f_1$) are recorded by the VNA using home-made software.

Data availability

The data that support the plots within this paper and other findings of this study are available from the corresponding authors upon reasonable request.

References

1. Wainstein, N., Adam, G., Yalon, E. & Kvatinsky, S. Radiofrequency switches based on emerging resistive memory technologies—a survey. *Proc. IEEE* **109**, 77–95 (2020).
2. Yalon, E. et al. Energy-efficient indirectly heated phase change RF switch. *IEEE Electron Device Lett.* **40**, 455–458 (2019).
3. Olsson, R. H., Bunch, K. & Gordon, C. Reconfigurable electronics for adaptive RF systems. In *2016 IEEE Compound Semiconductor Integrated Circuit Symposium (CSICS)* 1–4 (IEEE, 2016).
4. Lee, J.-L., Zych, D., Reese, E. & Drury, D. M. Monolithic 2-18 GHz low loss, on-chip biased PIN diode switches. *IEEE Trans. Microw. Theory Techn.* **43**, 250–256 (1995).
5. Larson, L. E. Integrated circuit technology options for RFICs-present status and future directions. *IEEE J. Solid-State Circuits* **33**, 387–399 (1998).
6. Li, Q., Zhang, Y. P., Yeo, K. S. & Lim, W. M. 16.6- and 28-GHz fully integrated CMOS RF switches with improved body floating. *IEEE Trans. Microw. Theory Techn.* **56**, 339–345 (2008).
7. Brown, E. R. RF-MEMS switches for reconfigurable integrated circuits. *IEEE Trans. Microw. Theory Techn.* **46**, 1868–1880 (1998).
8. Stefanini, R., Chatras, M., Blondy, P. & Rebeiz, G. M. Miniature MEMS switches for RF applications. *J. Microelectromech. Syst.* **20**, 1324–1335 (2011).
9. Patel, C. D. & Rebeiz, G. M. A compact RF MEMS metal-contact switch and switching networks. *IEEE Microw. Wireless Compon. Lett.* **22**, 642–644 (2012).
10. Wang, M. & Rais-Zadeh, M. Development and evaluation of germanium telluride phase change material based ohmic switches for RF applications. *J. Micromech. Microeng.* **27**, 013001 (2017).
11. Madan, H. et al. 26.5 terahertz electrically triggered RF switch on epitaxial VO_2-on-sapphire (VOS) wafer. In *2015 IEEE International Electron Devices Meeting (IEDM)* 9.3.1–9.3.4 (IEEE, 2015).
12. Pi, S., Ghadiri-Sadrabadi, M., Bardin, J. C. & Xia, Q. Nanoscale memristive radiofrequency switches. *Nat. Commun.* **6**, 7519 (2015).
13. Leon, A. et al. RF power-handling performance for direct actuation of germanium telluride switches. *IEEE Trans. Microw. Theory Techn.* **68**, 60–73 (2019).
14. El-Hinnawy, N., Slovin, G., Rose, J. & Howard, D. A 25 THz F_{CO} (6.3 fs $R_{ON}C_{OFF}$) phase-change material RF switch fabricated in a high volume manufacturing environment with demonstrated cycling > 1 billion times. In *2020 IEEE/MTT-S International Microwave Symposium (IMS)* 45–48 (IEEE, 2020).
15. Wong, H. S. P. et al. Metal–oxide RRAM. *Proc. IEEE* **100**, 1951–1970 (2012).
16. Wouters, D. J., Waser, R. & Wuttig, M. Phase-change and redox-based resistive switching memories. *Proc. IEEE* **103**, 1274–1288 (2015).

17. Field, M. et al. Vanadium dioxide phase change switches. In *Proc. SPIE 9479, Open Architecture/Open Business Model Net-Centric Systems and Defense Transformation 2015* 947908 (SPIE, 2015).
18. El-Hinnawy, N. et al. Origin and optimization of RF power handling limitations in inline phase-change switches. *IEEE Trans. Electron Devices* **64**, 3934–3942 (2017).
19. Ge, R. et al. Atomristor: nonvolatile resistance switching in atomic sheets of transition metal dichalcogenides. *Nano Lett.* **18**, 434–441 (2017).
20. Chappell, W. J., Hancock, T. M. & Olsson, R. H. Can phase change materials put the radio into software defined radio? In *2018 IEEE/MTT-S International Microwave Symposium—IMS* 829–831 (IEEE, 2018).
21. Kim, M. et al. Zero-static power radio-frequency switches based on MoS_2 atomristors. *Nat. Commun.* **9**, 2524 (2018).
22. Kim, M. et al. Non-volatile RF and mm-wave switches based on monolayer hBN. In *2019 IEEE International Electron Devices Meeting (IEDM)* 9.5.1–9.5.4 (IEEE, 2019).
23. Kim, M. et al. Analogue switches made from boron nitride monolayers for application in 5G and terahertz communication systems. *Nat. Electron.* **3**, 479–485 (2020).
24. Petrov, V., Kurner, T. & Hosako, I. IEEE 802.15.3d: first standardization efforts for sub-terahertz band communications toward 6G. *IEEE Commun. Mag.* **58**, 28–33 (2020).
25. Dang, S., Amin, O., Shihada, B. & Alouini, M.-S. What should 6G be? *Nat. Electron.* **3**, 20–29 (2020).
26. Chowdhury, M. Z., Shahjalal, M., Ahmed, S. & Jang, Y. M. 6G wireless communication systems: applications, requirements, technologies, challenges, and research directions. *IEEE Open J. Commun. Soc.* **1**, 957–975 (2020).
27. Tariq, F. et al. A speculative study on 6G. *IEEE Wireless Commun.* **27**, 118–125 (2020).
28. Yang, P., Xiao, Y., Xiao, M. & Li, S. 6G wireless communications: vision and potential techniques. *IEEE Netw.* **33**, 70–75 (2019).
29. Wu, X. et al. Thinnest nonvolatile memory based on monolayer h-BN. *Adv. Mater.* **31**, 1806790 (2019).
30. Shi, Y. et al. Electronic synapses made of layered two-dimensional materials. *Nat. Electron.* **1**, 458–465 (2018).
31. Zhao, H. et al. Atomically thin femtojoule memristive device. *Adv. Mater.* **29**, 1703232 (2017).
32. Lee, Y. H. et al. Synthesis and transfer of single-layer transition metal disulfides on diverse surfaces. *Nano Lett.* **13**, 1852–1857 (2013).
33. Hus, S. M. et al. Observation of single-defect memristor in an MoS_2 atomic sheet. *Nat. Nanotechnol.* **16**, 58–62 (2021).
34. Ge, R. et al. A library of atomically thin 2D materials featuring the conductive-point resistive switching phenomenon. *Adv. Mater.* **33**, 2007792 (2021).
35. Cha, J., Cha, J. & Lee, S. Uncertainty analysis of two-step and three-step methods for deembedding on-wafer RF transistor measurements. *IEEE Trans. Electron Devices* **55**, 2195–2201 (2008).
36. Liu, A.-Q. *RF MEMS Switches and Integrated Switching Circuits* (Springer Science & Business Media, 2010).
37. Zylbersztejn, A. & Mott, N. F. Metal-insulator transition in vanadium dioxide. *Phys. Rev. B* **11**, 4383 (1975).
38. Anagnostou, D. E., Torres, D., Teeslink, T. S. & Sepulveda, N. Vanadium dioxide for reconfigurable antennas and microwave devices: enabling RF reconfigurability through smart materials. *IEEE Antennas Propag. Mag.* **62**, 58–73 (2020).
39. Hillman, C., Stupar, P. & Griffith, Z. Scaleable vanadium dioxide switches with submillimeterwave bandwidth: VO_2 switches with impoved RF bandwidth and power handling. In *2017 IEEE Compound Semiconductor Integrated Circuit Symposium (CSICS)* 1–4 (IEEE, 2017).
40. Lee, S. et al. 300-GHz CMOS-based wireless link using 40-dBi Cassegrain antenna for IEEE Standard 802.15.3d. In *2020 IEEE International Symposium on Radio-Frequency Integration Technology (RFIT)* 136–138 (IEEE, 2020).
41. Cascade Microtech Application Note. *On Wafer Vector Network Analyzer Calibration and Measurements*. (Publication Name PYRPROBE-0597, 1997).

Acknowledgements

This work was supported in part by the Office of Naval Research (grant N00014-20-1-2104) and the Air Force Research Laboratory (award FA9550-21-1-0460). D.A. acknowledges the Presidential Early Career Award for Scientists and Engineers (PECASE) through the Army Research Office (award W911NF-16-1-0277). The fabrication was partly done at the Texas Nanofabrication Facility supported by NSF grant NNCI-1542159. M.K. acknowledges the UK Brand Research Fund (1.220028.01) of UNIST. E.P. acknowledges funding from the ANR SWIT project (ANR-19-CE24-0004). The data communication setup used for the BER measurements was partially funded by an ANR TERASONIC grant, Contrat de Plan Etat-Region (CPER) Photonics for Society (P4S) and DYDICO cluster of the I-site ULNE. The development of some parts of the setup was also enabled using devices from RENATECH, the French nanofabrication network. The THz communication setup is also supported by the ANR SPATIOTERA project, TERIL-WAVES project, Nano-FUTUR Equipex Program (ANR-21-ESRE-0012) of the 'Plan d'Investissement d'Avenir (PIA)' and also supported by the IEMN UHD Flagship and CPER WaveTech@HdF.

Author contributions

M.K. performed the material transfer, characterization, device fabrication and low-frequency measurements. E.P., G.D. and S.S. contributed to the high-frequency measurements. G.D., E.P. and P.S. conducted the BER, SNR, eye diagram and constellation diagram measurements. N.W., K.S. and E.Y. contributed to the pulse measurement of the MoS_2 device. M.K., S.J.Y., E.P., G.D. and D.A. analysed the electrical data and characteristics. All the authors contributed to the article based on the draft written by M.K., E.P., G.D. and D.A. E.Y., E.P., H.H. and D.A. initiated and supervised the collaborative research.

Competing interests

The authors declare no competing interests.